

Delft University of Technology

Rotor wake aerodynamics assignment 1

BEM model of a wind turbine

Changkyu Park 4646061

Cihangir Özbek 4448146

Malte Wegener 4672194

Submission Date: March 25, 2021

Course: AE4135

Group: 25

Contents

1	Introduction	2
2	Flowchart of the program	2
3	Blade Element Momentum Theory	2
4	Results	3
4.1	Axial operating condition	3
4.2	Yawed operating condition	6
4.3	Influence of the tip correction	12
4.4	Influence of the number of annuli	12
4.5	Influence of spacing method	13
4.6	Convergence history of total thrust	14
5	Distribution of stagnation enthalpy	14
6	System of circulation	16
7	Operational point of the airfoil	17
8	Conclusion	18

1. Introduction

The Blade Element Momentum (BEM) model is programmed for a heavily loaded wind turbine in axial and yawed flow in this assignment. The Prandtl tip and root corrections, as well as the Glauert correction were implemented to better represent the system under analysis to account for the hub of the turbine, tip-loss and the yaw angle. In this report, a flowchart of the program representing the iterative computation is presented, together with the various results of the wind turbine's performance characteristics.

2. Flowchart of the program

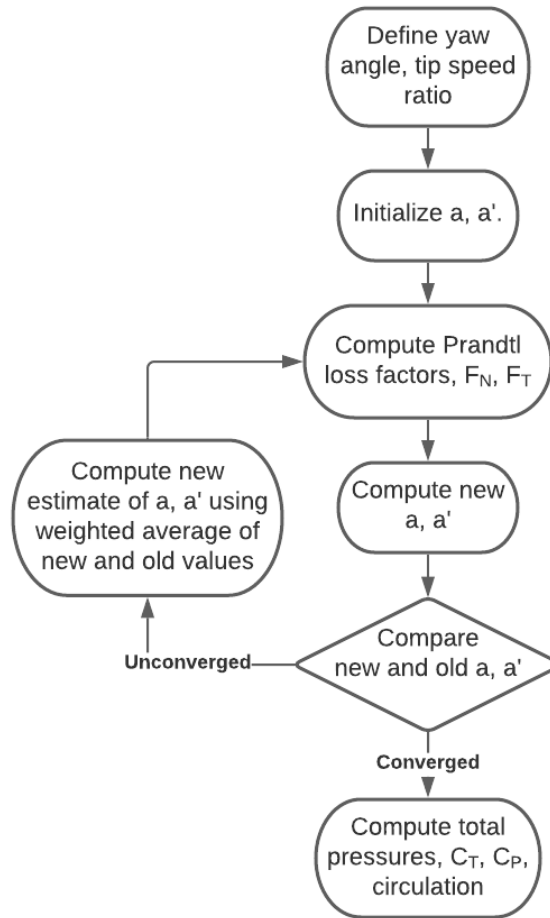


Fig. 1 Flowchart of the program set up and used

3. Blade Element Momentum Theory

BEM Theory is a combination of two separate theories: Momentum theory and Blade element theory (strip theory). To discuss the main assumptions of BEM theory, the assumptions made in each individual theory should first be mentioned and elaborated. Momentum theory is applied to a streamtube with an actuator disk that creates a pressure drop in the flow. The boundaries of the control volume are defined by the surface of the stream tube and the inlet and outlet. When applying this momentum theory, the following assumptions are made:

- 1) Steady state, inviscid, incompressible, uniform one dimensional flow
- 2) Constant internal energy
- 3) The static pressure at the inlet and outlet of the stream-tube is equal to the undisturbed ambient static pressure
- 4) Infinite number of blades (actuator disk)
- 5) No frictional drag

The three governing equations used in momentum theory is conservation of mass, momentum and energy. The fact that we assume steady state allows us to discard any terms that include time derivatives in the conservation equations. This simplifies the analysis significantly. Assuming that the flow is inviscid adds to the simplification of the conservation laws, the viscous terms can be neglected. Incompressibility allows us to simplify the continuity equation, it means that density is constant everywhere in the control volume. Together with the fact that we assume constant internal energy, the energy equation reduces to the Bernoulli equation.

The assumptions that we made so far helped us simplify the conservation equations. Now, when we assume that the flow is uniform and one dimensional together with the assumption that the static pressure at the inlet and outlet is equal to the ambient pressure, the evaluation of the conservation laws become much easier. The maximum power coefficient that is achievable with momentum theory is $16/27$ (Betz limit). However, during the analysis we neglected drag and the fact that we have an actuator disk and thus neglect any losses that come from the fact in reality we have a limited number of blades.

These were the assumptions made for solely the momentum theory. When using momentum theory in relation BEM, the disk is divided in several annuli where moment theory is applied on. It is assumed that there is no cross-flow so that the annuli are independent of each other. This is also done in blade element theory, each blade element is assessed individually, so there is no radial interaction. This is again a simplification of reality.

4. Results

4.1. Axial operating condition

The spanwise variation of the angle of attack and inflow angle is plotted for different tip speed ratios (TSR) in Figure 2.

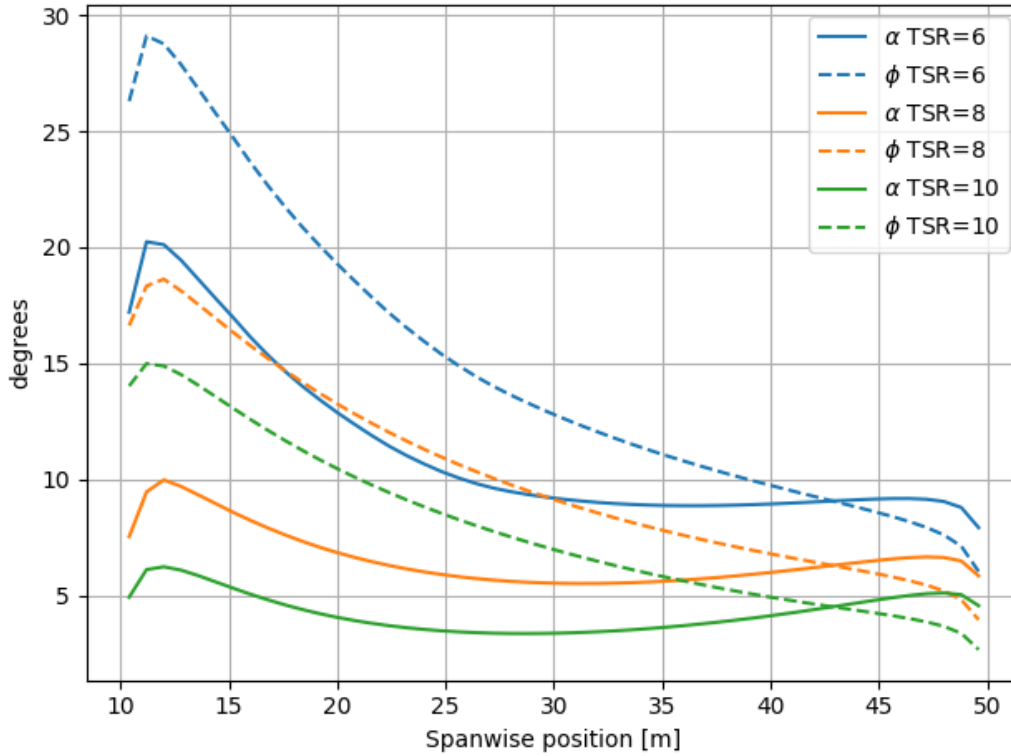


Fig. 2 Spanwise variation of angle of attack and inflow angle

It can be seen that the inflow angle decreases with the span position, which is expected. When comparing the inflow angle for the different TSRs, one can see that having a TSR of 6 results in quite high inflow angles at the root compared to the rest of the blade. For TSR of 8 and 10, the same is observed. However, it is not as extreme as it was for the low TSR case.

Similar to the inflow angle, the angle of attacks decreases with the spanwise location. However, around the middle of the blade, it increases again. The inflow angle is the sum of the angle of attack, the pitch angle and the twist. Pitch is constant, and the twist of this blade is positive at the root and it linearly decreases to zero degrees at the tip. Thus at the end, the angle of attack and inflow angle are related by the twist distribution of the blade. Again for a TSR of 6, in the root region till around $0.3r/R$, the angle of attack is in the stall region and this part of the blade is thus expected to be less efficient. It can also be observed that the higher the TSR, the closer the minimum and the maximum angle of attack are coming together. This implies a much more constant C_l/C_d ratio along the blade. For both the inflow angle and the angle of attack, the effects of tip and root corrections can be seen for all TSRs.

Furthermore, the axial and tangential induction factor is plotted in Figure 3.

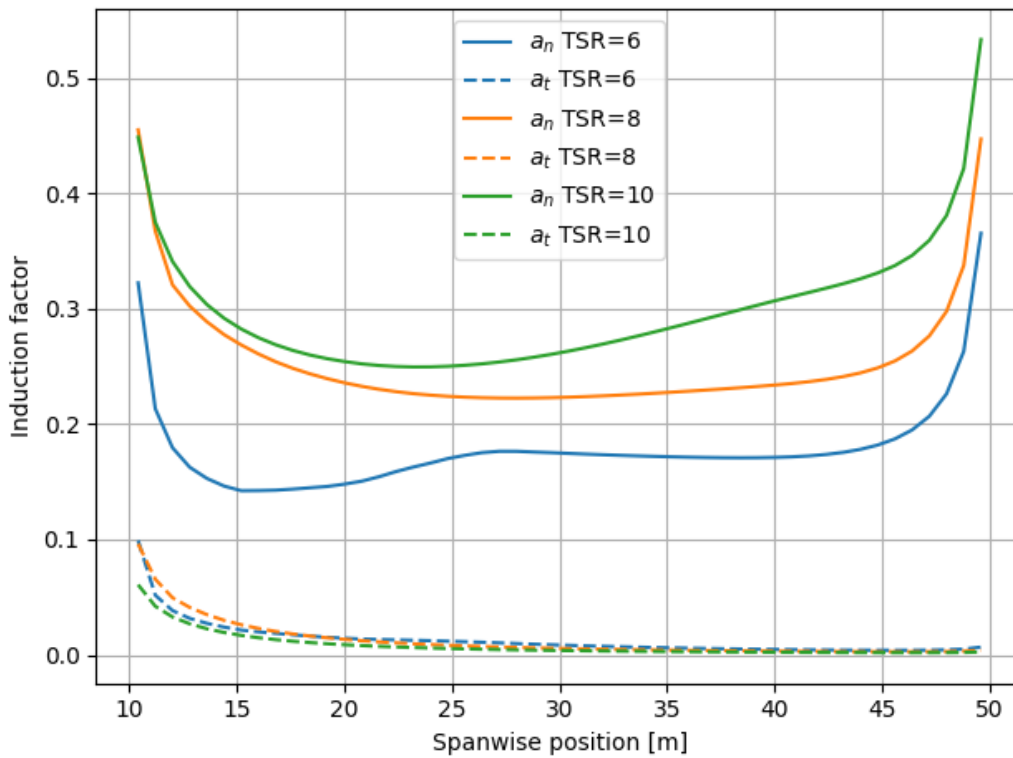


Fig. 3 Spanwise variation of axial and azimuthal induction factor at the rotor disk

It can be seen that the axial induction follows the known pattern of the lectures and increases with TSR. The tangential induction factor is significantly smaller than the axial one and decreases with TSR. Also, the tip and root corrections are more prominent here compared to Figure 2. For the tangential induction factor, the TSR does not affect the shape of the spanwise distribution. The same cannot be said for axial induction. When we neglect the tip and root region, around $r = 30m$ the axial induction factor is constant and for lower r , it is decreased. For TSR equal to 8, the axial induction factor is somewhat constant. At the highest TSR, we see the opposite of what is happening at the lowest TSR. The closer one gets to tip the induction factor increases.

Next, the actual force on the rotor is shown in Figure 4.

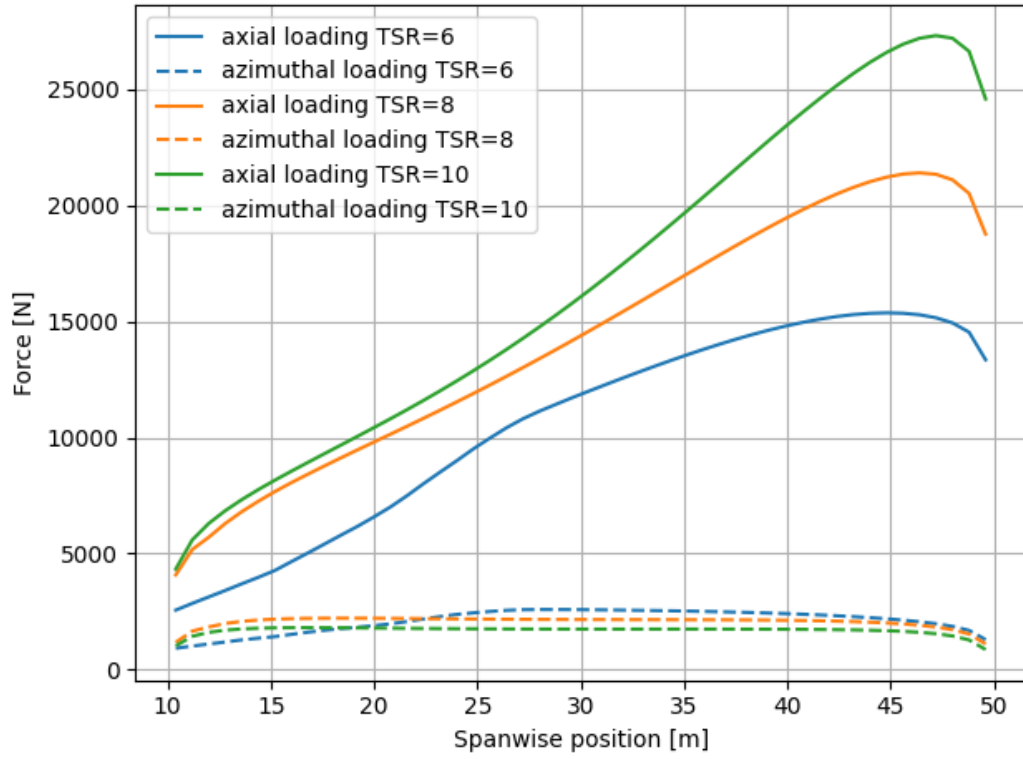
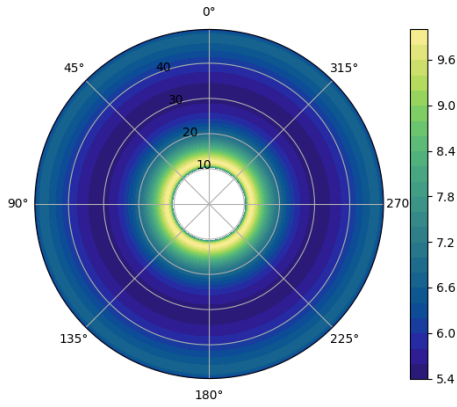


Fig. 4 Spanwise variation of axial and azimuthal loading of the rotor disk

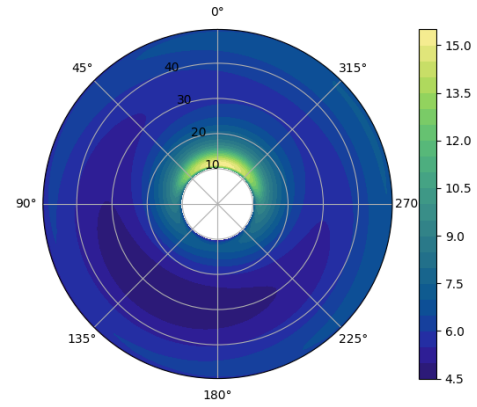
It can be seen that the axial loading is significantly stronger than the azimuthal loading. The axial loading increases with TSR and with spanwise position. On the other hand, the azimuthal loading stays near constant over the span.

4.2. Yawed operating condition

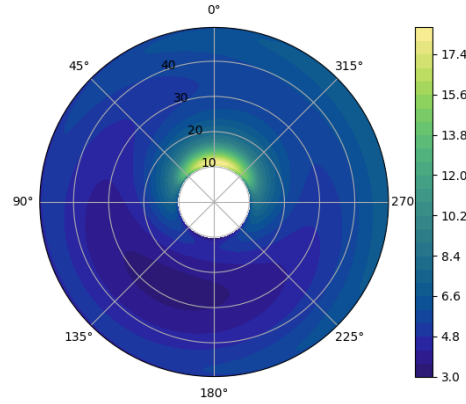
In Figure 5 and Figure 6 the azimuthal and spanwise variation of angle of attack and inflow angle is shown, when looking at the rotor from the front of a turbine that has the rotor turned to the left (counter-clockwise) when looking from above.



(a) Variation of angle of attack at 0 degree yaw

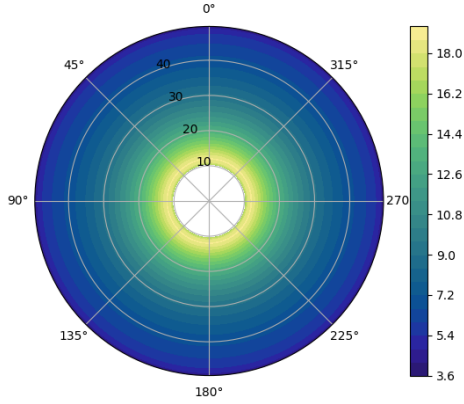


(b) Variation of angle of attack at 15 degree yaw

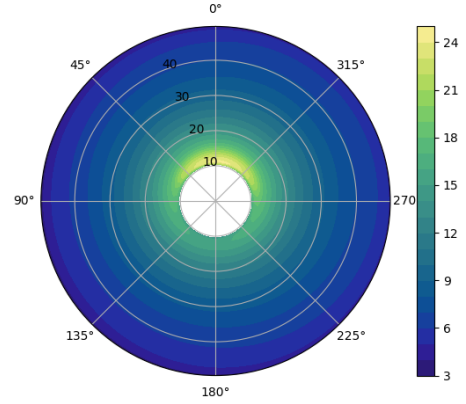


(c) Variation of angle of attack at 30 degree yaw

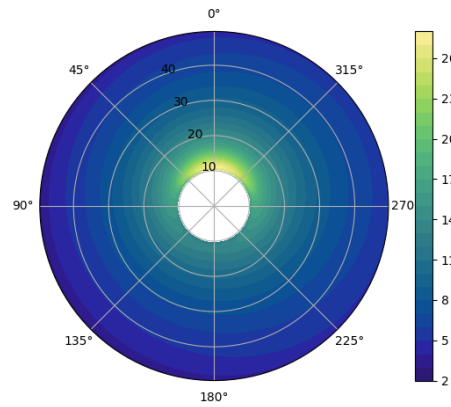
Fig. 5 Polar plot of angle of attack for different yawed operating conditions at a TSR of 8



(a) Variation of inflow angle at 0 degree yaw



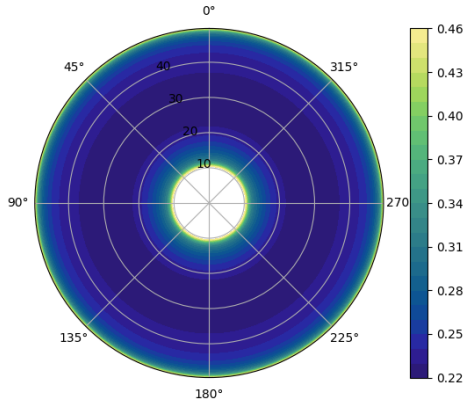
(b) Variation of inflow angle at 15 degree yaw



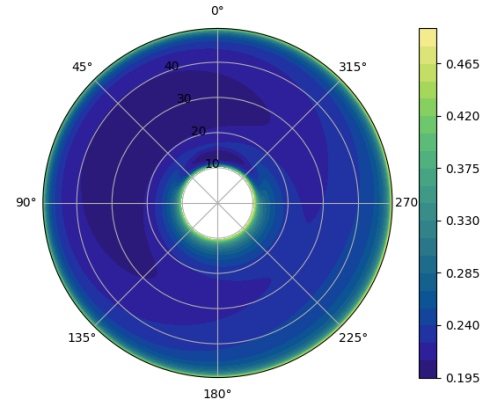
(c) Variation of inflow angle at 30 degree yaw

Fig. 6 Polar plot of inflow angle for different yawed operating conditions at a TSR of 8

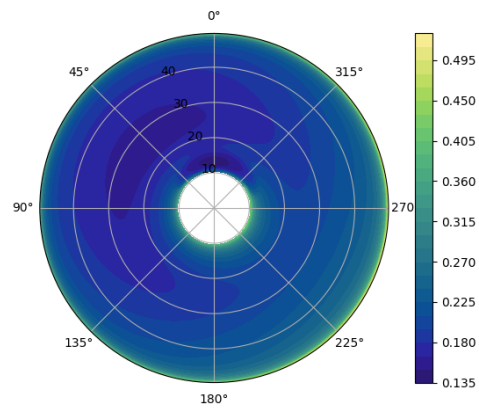
It can be seen that the general trend of the non-yawed condition can be observed. However, around the 0-degree azimuth, the inflow angle and the angle of attack are increased while on the opposite side they are decreased. This outcome is expected from the flow conditions. The axial and tangential induction factors are plotted in Figure 7 and Figure 8.



(a) Variation of axial induction factor at 0 degree yaw

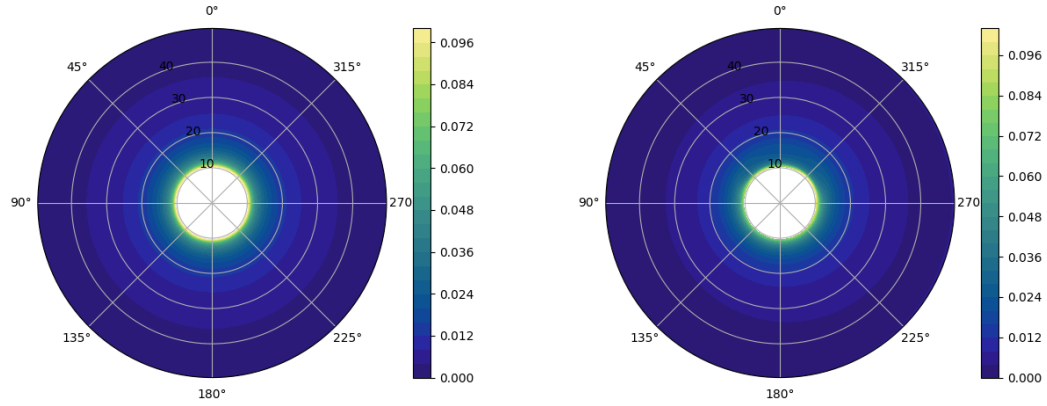


(b) Variation of axial induction factor at 15 degree yaw

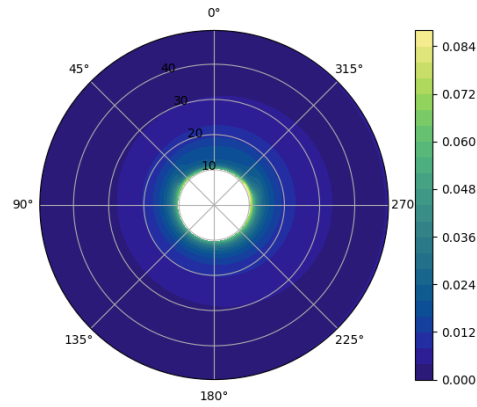


(c) Variation of axial induction factor at 30 degree yaw

Fig. 7 Polar plot of axial induction factor for different yawed operating conditions at a TSR of 8



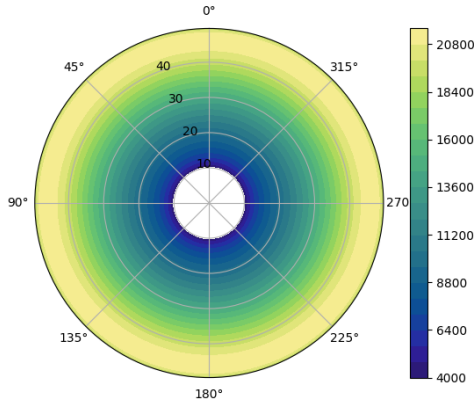
(a) Variation of tangential induction factor at 0 degree yaw (b) Variation of tangential induction factor at 15 degree yaw



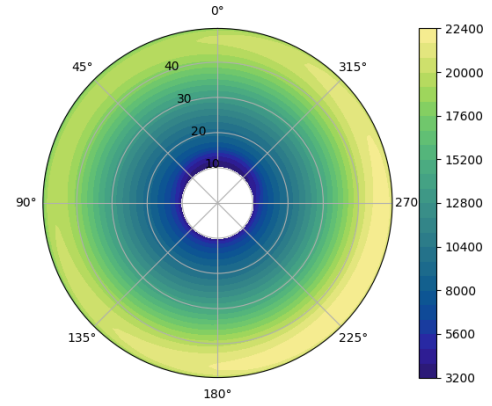
(c) Variation of tangential induction factor at 30 degree yaw

Fig. 8 Polar plot of tangential induction factor for different yawed operating conditions at a TSR of 8

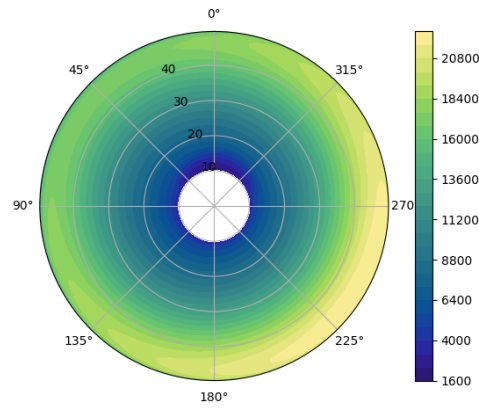
The axial induction factor shows a strong dependence on the yaw angle, while the tangential induction is affected significantly less. It can be seen that the leeward side of the rotor is loaded stronger than the windward side of the rotor. The distribution of axial and tangential forces is shown in Figure 9 and Figure 10.



(a) Variation of Thrust [N] at 0 degree yaw

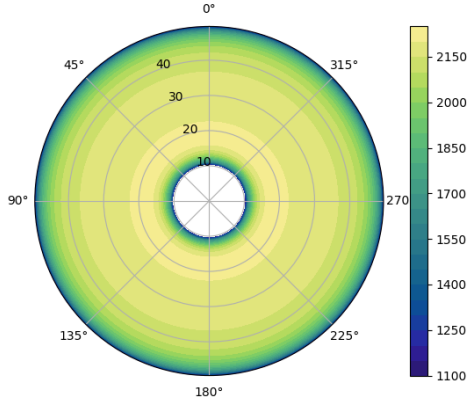


(b) Variation of Thrust [N] at 15 degree yaw

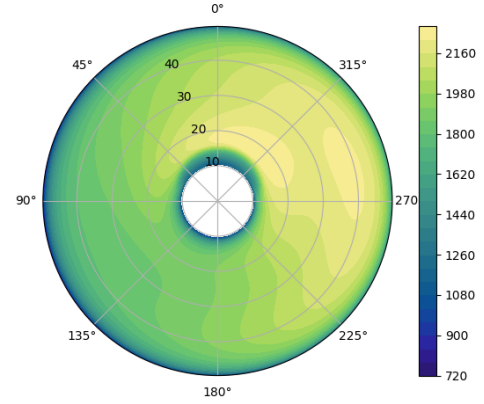


(c) Variation of Thrust [N] at 30 degree yaw

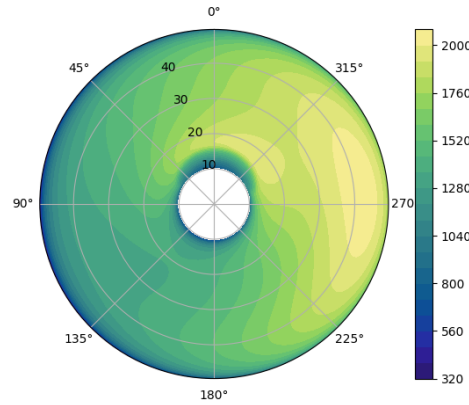
Fig. 9 Polar plot of Thrust [N] for different yawed operating conditions at a TSR of 8



(a) Variation of azimuthal force [N] at 0 degree yaw



(b) Variation of azimuthal force [N] at 15 degree yaw



(c) Variation of azimuthal force [N] at 30 degree yaw

Fig. 10 Polar plot of azimuthal force [N] for different yawed operating conditions at a TSR of 8

In the figures, similar patterns to the induction factors can be seen especially for the thrust force. Furthermore, stronger loading near the tips can be observed. The azimuthal force varies from the tangential induction factor and displays stronger effects on the leeward side than on the windward side, which was expected.

4.3. Influence of the tip correction

The influence of the tip correction on the induction factors has been presented in Figure 11. It can be observed near the tip of the spanwise position that the axial induction factor a_n is significantly affected by introducing no tip correction. Instead of rising to a value similar to the value at root, it maintains its magnitude approximately. However, as for the azimuthal induction factor a_t , there is minimal difference introduced due to the absence of the tip correction.

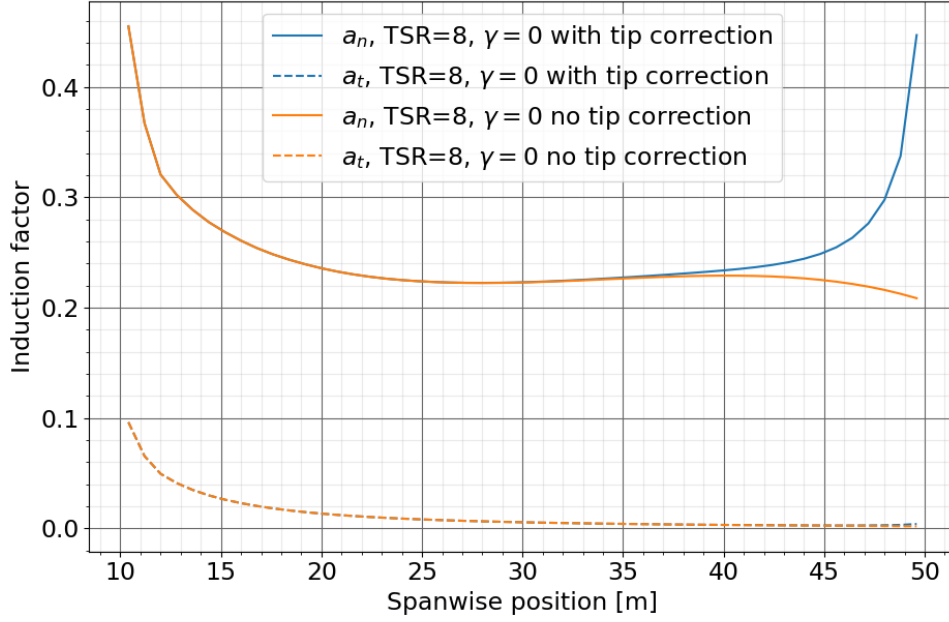


Fig. 11 Influence of tip correction on the induction factors

4.4. Influence of the number of annuli

To analyse the influence of the number of annuli on the thrust loading C_T , results from 2 to 500 annuli were computed and plotted in Figure 12 on a log-log scaled axes.

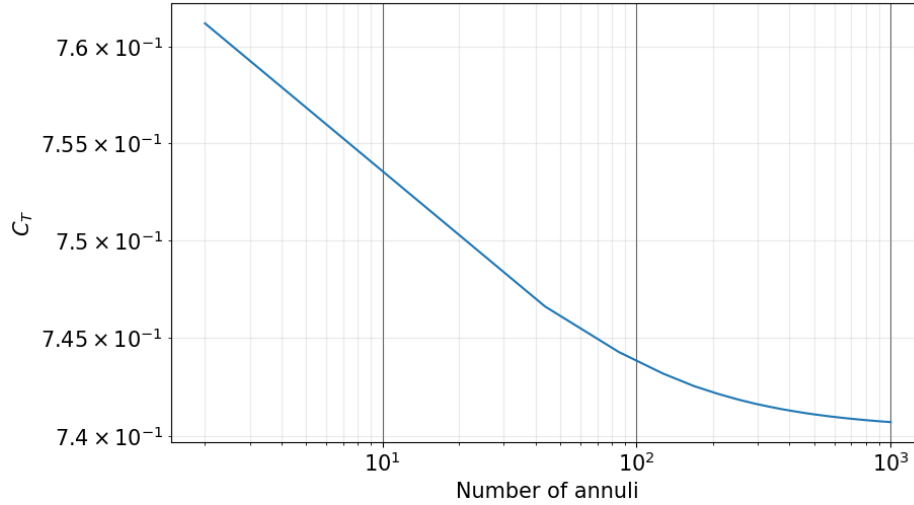


Fig. 12 Influence of number of annuli on the loadings at $TSR = 8$ without yaw

The magnitude of the thrust loading decreases minimally with an increase in the number of annuli, implying the reduction in discretization error introduced with a low number of annuli. It is also observed that the C_T slowly converges

at around 1000 annuli. However, the computing resource required to increase from 500 to 1000 annuli does not seem worth the small reduction in error.

4.5. Influence of spacing method

Instead of using the conventional constant spacing method, cosine spacing was implemented as well to analyse the influence of the spacing method on the loading. Cosine spacing increases the density of nodes at the ends while decreasing it in the middle. The comparison is then shown in the plot of Figure 13.

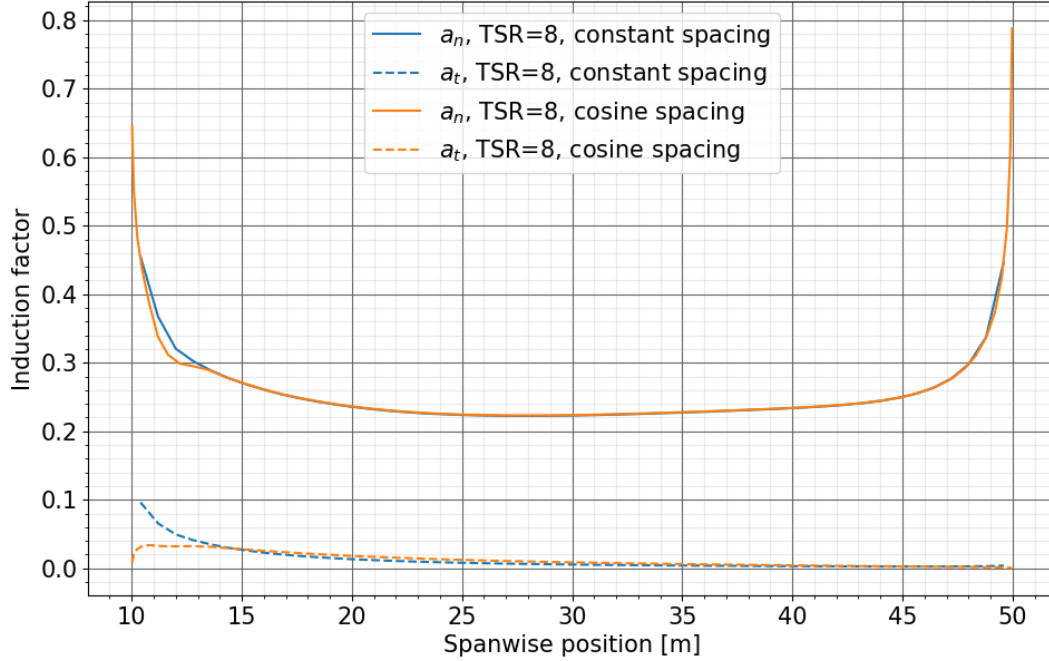


Fig. 13 Influence of spacing method, constant vs. cosine spacing at $TSR = 8$ without yaw

It is observed that both methods yield consistent results, with the cosine spacing achieving better resolution of the induction factors close to the root and tip where the points of the cosine spacing method are concentrated.

4.6. Convergence history of total thrust

The total thrust for each iteration during the iterative process has been recorded and plotted on log-log scaled axes as shown in Figure 14 for the maximum allowed error of 10^{-7} for the induction factors in the program.

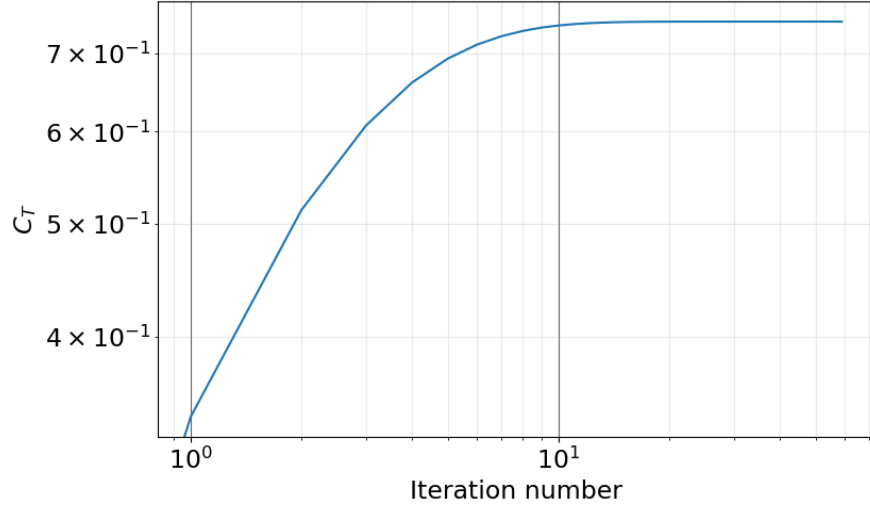


Fig. 14 Convergence history of total thrust at TSR= 8 without yaw

A second-order increase in C_T is observed in the early stage of iteration which then gradually decreases and finally converging around iteration number 100, from which the iteration is furthered to meet the maximum allowed error requirement.

5. Distribution of stagnation enthalpy

The stagnation enthalpy is defined as the sum of static and dynamic pressure:

$$h = p + 0.5\rho V^2$$

It can be seen as a measure of how much energy is present in the flow. For the velocity components at the rotor disk and in the far-field, we use the results from momentum theory:

$$U_D = U_\infty (1 - a) \quad \& \quad U_W = (1 - 2a)$$

To find the static pressure just before and after the rotor, Bernoulli's equation is used. For the static pressure before the disk, Bernoulli's equation is used between the inlet of the streamtube and just before the disk. To find the static pressure just after the rotor, the same is done but now the outlet of the streamtube is used. These results are shown in Figure 15.

As one can see, the highest enthalpy is found at the inlet ($-\infty$) which is expected. The enthalpy has dropped just before the disk. From momentum theory, we know that static pressure increases and velocity decreases when one moves closer to the rotor from the inlet. What we thus see is that the decrease in velocity has a more significant effect on the enthalpy than the increase in static pressure. This we see mostly in the middle of the blade. At the tip and root, the blade sees a lower enthalpy drop. Just after the rotor, the enthalpy is the lowest, which is expected since the rotor causes a pressure drop. Here we can also see that the tip and root regions are less effective. At the outlet of the streamtube ($+\infty$), the enthalpy has increased again. As we can see for the enthalpy just before the rotor, the velocity has a bigger influence on enthalpy than the static pressure. The static pressure contribution is the same as for ($-\infty$), however, the difference between $-\infty$ and $+\infty$, is the dynamic pressure contribution. This is for $+\infty$ lowered by a factor of $(1 - 2a)^2$

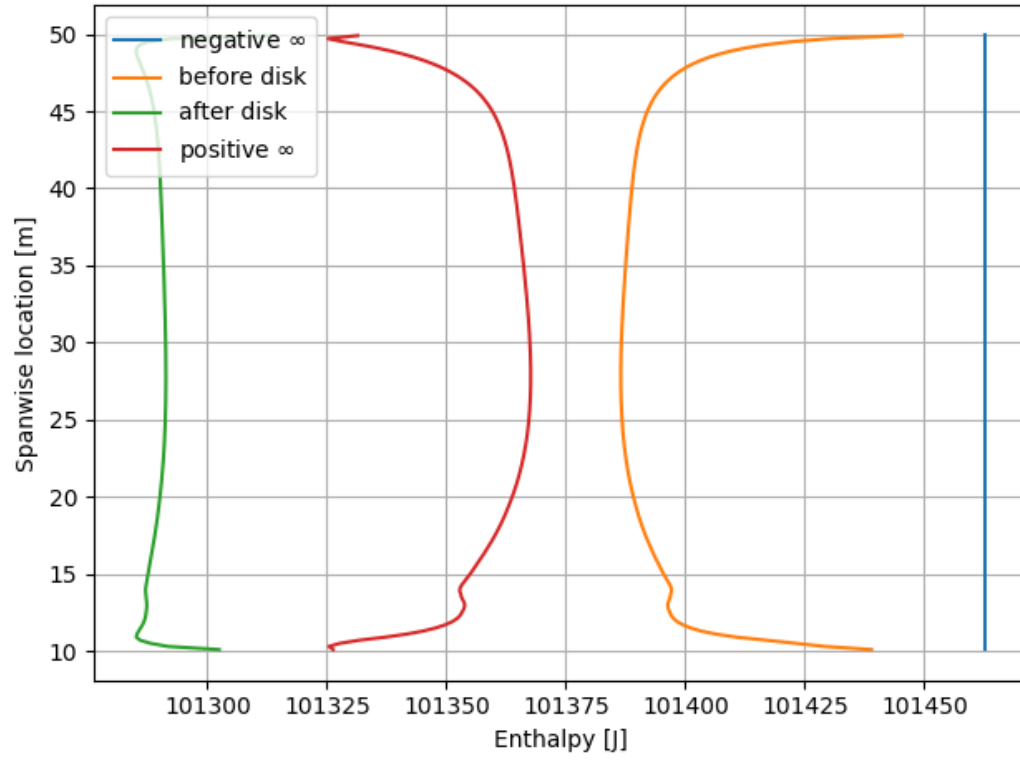


Fig. 15 Spanwise variation of stagnation enthalpy

6. System of circulation

The spanwise distribution of circulation for three different yaw configuration at TSR= 8 are presented in Figure 16 and they are namely: $\gamma = 0, 15$ and 30 degrees.

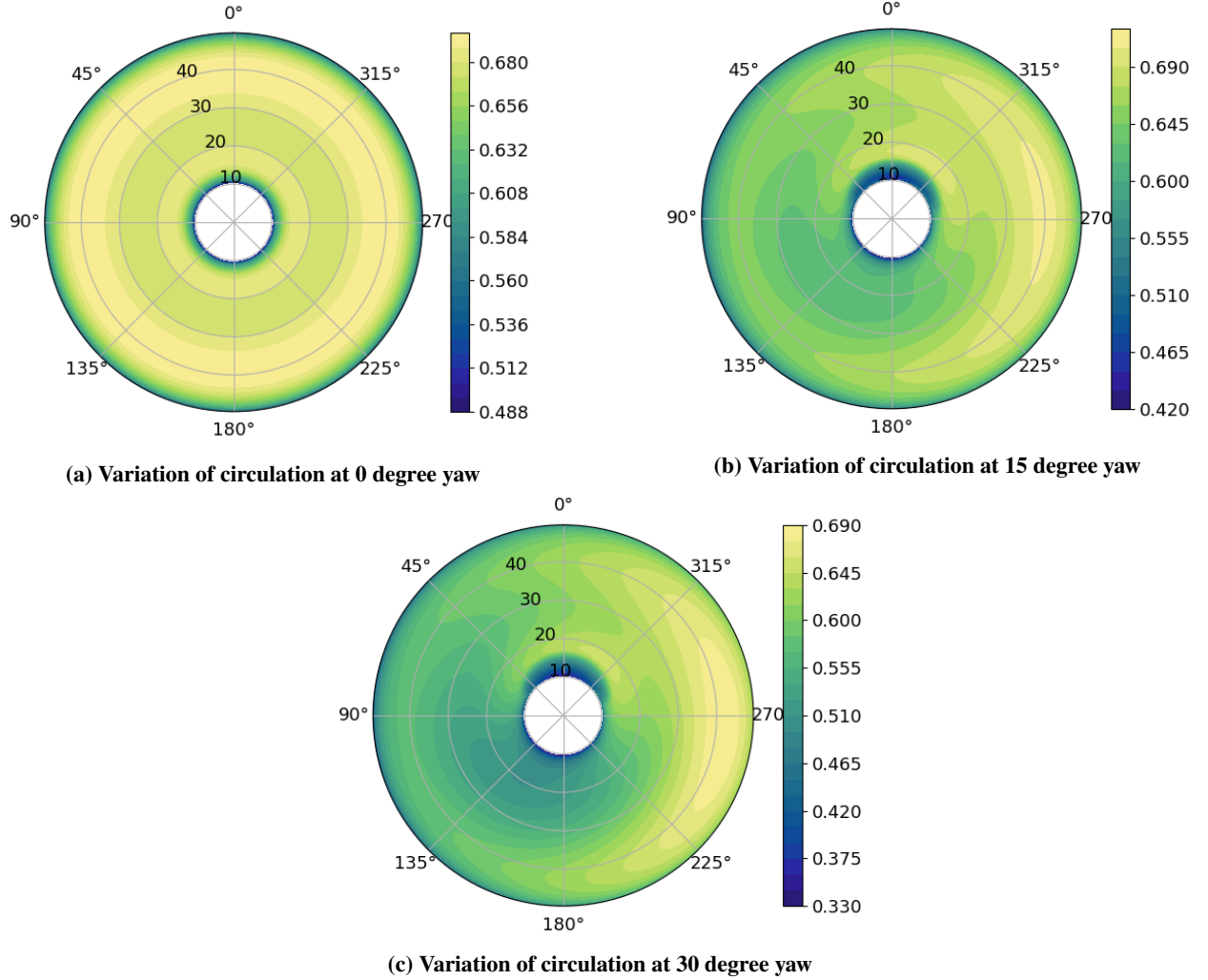


Fig. 16 Polar plot of circulation for different yawed operating conditions at a TSR of 8

Starting with 0-degree yaw, it can be observed that every azimuth angle features the same spanwise distribution of circulation. For each of the azimuth angle, the lower magnitudes of circulation exist at and close to the root and tip of the span while the remaining regions have higher values. With yaw introduced, the overall magnitude of the circulation decreases within the span, especially at the side that enters the flow first (windward side). Furthermore, the lower limit of the magnitude near the root covers a larger area in the top region. With an increase in yaw angle, this same effect is amplified.

7. Operational point of the airfoil

At the beginning of the report, the relation between the inflow angle and angle of attack was shortly discussed. It was mentioned that a constant angle of attack along the blade would give a certain constant C_l/C_d ratio. For an optimum C_p , one would like to minimise the drag losses since drag has a negative effect on the amount of torque produced by the blade. So one design approach is to find the angle of attack that maximises C_l/C_d , and use this angle of attack along the whole blade [1]. From the constant C_L and the varying λ_r , one can calculate the shape of the blade (its chord and twist distribution). For low TSRs, this will result in blades with a large chord and for high TSRs, this will result in long and slender blades [1].

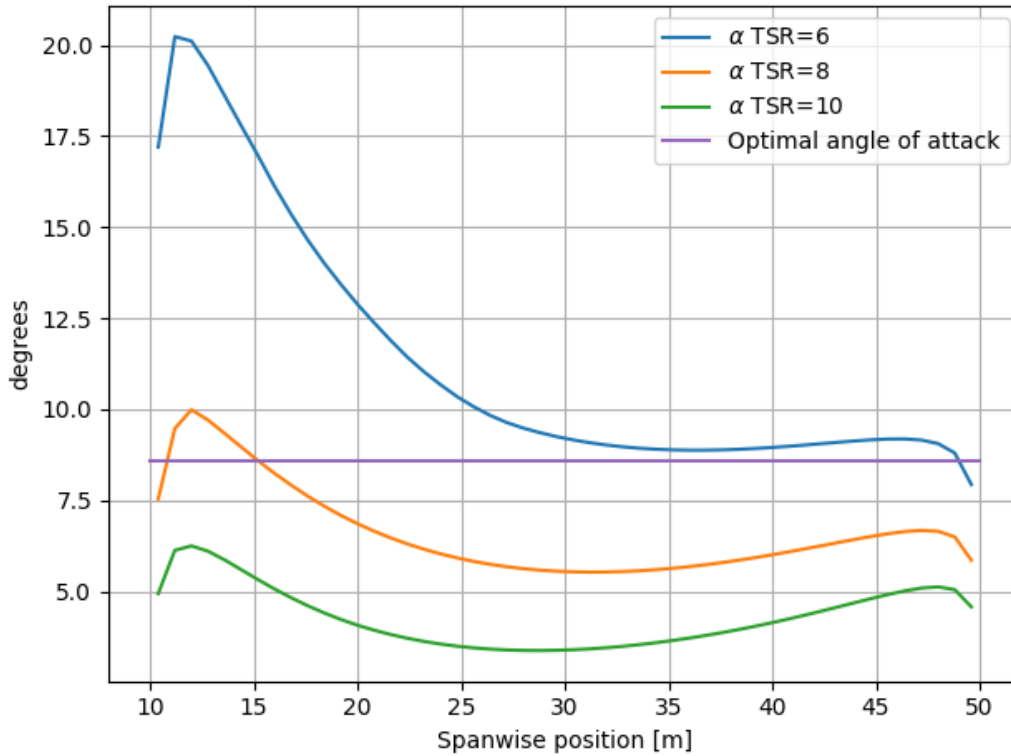


Fig. 17 Spanwise variation of angle of attack vs optimal angle of attack of the airfoil for maximum lift over drag ratio

It is not always possible to manufacture the desired chord distribution that comes from this analysis. So one can also begin the analysis with a certain chord distribution and calculate the desired angle of attack from here, which means that there is no constant C_L/C_D and angle of attack [1].

8. Conclusion

It can be concluded, that an increase in tip speed ratio (TSR) increases the loading of the wind turbine with drastic increments in the angle of attack and inflow angle, especially near the root of the span. On the other hand, introducing yaw decreases both its axial and azimuthal forces, ultimately reducing its performance. It was also realised that the absence of tip correction had a huge adverse effect on the computation of the induction factor, giving a high inaccuracy near and at the tip. Moreover, the implementation of cosine spacing instead of constant spacing had a positive impact on the analysis by increasing accuracy at the ends, the root and the tip. Along a streamtube there are several changes in enthalpy. The highest enthalpy is at the inlet, just before the rotor the enthalpy has decreased and just after the rotor the enthalpy is at its lowest. Moving towards the outlet the enthalpy increases again. The circulation distribution was also affected by yaw, with a smaller magnitude of circulation developing at the windward side of the rotor with increasing yaw angle. When designing a rotor for maximum power, the optimum blade design is achieved by having a constant angle of attack along the blade, sometimes this is structurally not feasible and thus the angle of attack can vary.

References

- [1] *Aerodynamics of Horizontal-Axis Wind Turbines*, John Wiley & Sons, Ltd, 2001, Chap. 3, pp. 41–172.